A thermo-hydro-mechanical model to evaluate the seismic properties of geothermal reservoirs

Nianqi Li[1], Li-Yun Fu[2], Wubing Deng[2], José M. Carcione[3], and Jian Yang[1]

ABSTRACT

Fractured-vuggy thermal reservoirs with complex pore spaces (stiff pores, cracks, and fractures) are typical geothermal resources for development and utilization in China. The cyclic recovery of such thermal reservoirs involves a complex thermo-hydro-mechanical (THM) coupling process. Insights into the thermoelastic effects of heating-cooling cycles on the seismic response have great potential for seismic monitoring in the cyclic recovery, which remains largely unaddressed in the literature. We intend to fill this gap by applying the double-porosity thermoelasticity theory to interpret ultrasonic measurements on granite under water-cooling conditions. We consider an isotropic porous host embedded with fractures. A plane-wave analysis yields the classical P and S waves and three slow P waves, namely the slow (Biot) P1, the slow (Biot) P2, and a thermal P. We investigate the combined effect of temperature, porous structure, and pore fluid on the thermoelastic properties of the THM process for typical granite reservoirs that experience a cold-shock process. Fractures provide the main channels for heat exchange and fluid flow. Our THM thermoelastic model describes the reservoir properties as a function of temperature associated with thermal-induced cracking, where fracture porosity is more important than the stiff (host) pore to describe the reservoir quality. We find that the thermal conductivity and specific heat have negligible effects in the seismic frequency band for the temperature range of less than 400°C, whereas the crack density significantly affects the seismic response in the heating-cooling cycles because of the additional contribution of thermal- and cold-shock-induced cracks. We further determine that the P-wave velocity and attenuation due to thermal effects under water cooling offer an important index to monitor the thermal-induced cracking and operation efficiency of the enhanced geothermal system. The THM thermoelastic model lays the foundation for active (or passive) seismic monitoring of the cyclic recovery of thermal reservoirs.

INTRODUCTION

Geothermal energy is one of the important solutions to reducing carbon emissions. In recent years, an enhanced geothermal system (EGS), as an economic development pattern of the geothermal resource, has been widely used for recovering geothermal energy from subsurface reservoirs by creating an artificial circulation system of fluid (e.g., water or CO_2) through fracturing techniques to enhance the porosity and permeability of hot dry rocks. In a typical EGS, the temperature is usually more than 200°C, with water used as a heat-transfer fluid (e.g., Breede et al., 2013; Olasolo et al., 2016).

Significant differences in temperature between injected cold water and the host formation often induce cracks due to cold-shock effects (e.g., Collin and Rowcliffe, 2002; Kang et al., 2021; Fan et al., 2022). The resulting cracks may help to improve the permeability of rocks, enhancing the heat exchange efficiency (Hu et al., 2021).

Various seismic techniques (including active and passive surveys) have been widely used to investigate subsurface conditions of geothermal resources (Willis et al., 2010), including real-time seismic monitoring to evaluate the operational efficiency and stability of thermal reservoirs (Berard and Cornet, 2003), induced seismicity in geothermal systems (e.g., Majer et al., 2007; Buijze et al.,

2019; Cacace et al., 2021), azimuthal anisotropy by geothermal resource potential using a 3D-3C seismic survey (Kent et al., 2013), characterization of ambient seismic noise near a deep geothermal reservoir (Lehujeur et al., 2015), and high-resolution 3D seismic imaging of fracture networks of a deep geothermal reservoir (Salaun et al., 2020). These studies focus on the application of seismic techniques, which generally requires a proper understanding of temperature-dependent physical properties in geothermal reservoirs and associated impacts on the seismic response.

Granite is a typical source rock for geothermal reservoirs, with its microstructures altered by cold-water injection of EGS or by heating-cooling cycles in experimental measurements. The ultrasonic wave test is commonly used to detect the interior failure of rocks because of its simple and nondestructive characteristics. Numerous experimental studies have been conducted to investigate the sensitivity of seismic properties to temperature variations (e.g., Batzle and Wang, 1992; Yang et al., 2019, 2021; Qi et al., 2021). Poletto et al. (2018) present a theory and sensitivity analysis based on the Burgers model for brittle-ductile behavior, integrated with a modified Gassmann model for fluid-saturated porous rocks, pressure effects for bulk and shear moduli, as well as permeability and squirt flow effects.

Acoustic velocities in rocks are very sensitive to thermal-induced microcracking (e.g., Wang et al., 1989). Based on the Drucker-Prager and Mohr-Coulomb failure criteria, Yang et al. (2022a) propose a coupled thermo-mechanical damage model of granite in terms of P-wave velocities as a function of temperature under heating-cooling cycles. The thermo-mechanical coupling of rocks during heating-cooling cycles is generally characteristic of the Kaiser effect or thermal memory (Kaiser, 1950; Zuberek et al., 2002; Wang et al., 2020), which includes three phases: thermal memory acquisition, retention, and fading. Numerous measurements (e.g., Griffiths et al., 2018; Shi et al., 2020) under heating-cooling cycles are indicative of extensive thermal microcracking during the first cycle (i.e., memory acquisition), predominantly during the heating phase that causes a dramatic decrease of P- and S-wave velocities with temperature. The reduced microcracking is observed during the second cycle and less still during the third cycle, where the apparent decrease in velocity with temperature is almost reversible. That is, the subsequent heating-cooling cycles will not significantly affect the thermo-mechanical properties of granite unless a higher temperature is applied. Our study actually focuses on the thermoelastic effect during the first cycle.

Geothermal reservoirs particularly with the EGS for cyclic recovery are usually characterized by multiscale pore structures. For instance, fractured-vuggy karst thermal reservoirs are a typical geothermal resource in China, with the advantage of large water output and easy recharge of tailwater after its utilization (Yao et al., 2022). Such fractured-vuggy reservoirs have complex pore spaces (e.g., stiff pores, fractures, and vugs) and involve a complex thermo-hydro-mechanical (THM) coupling process in the cyclic recovery (e.g., Chen et al., 2014; Yao et al., 2018, 2022; Zhang et al., 2021). For such double-porosity reservoirs, the thermoelastic effect on the seismic response remains largely unaddressed in the literature. We address this issue by using a double-porosity thermoelasticity (DPT) theory (Li et al., 2022). The theory predicts the presence of two Biot slow modes (i.e., Biot slow P1 and Biot slow P2) and thermal slow P wave (i.e., T mode) in addition to the classical fast P and S waves. The former three modes correspond

to two attenuation mechanisms of thermoporoelasticity: local-heat flow and local-fluid flow (LFF) due to wave propagation, respectively. The frequency-dependent attenuation curves (Li et al., 2022) show that these slow waves manifest as Zener-like relaxation peaks. The viscosity and thermoelasticity properties can lead to the diffusive behavior of the three slow P modes.

Li et al. (2022) use the DPT model to describe experimental and logging data with monotonic changes in temperature, where pore structures and fluid parameters are fixed. In this study, we use the DPT model to build the THM thermoelastic model subject to heating-cooling cycles, which describes the reservoir properties as a function of the temperature associated with thermal-induced cracking. The proposed THM thermoelastic model relates thermoelastic parameters (moduli, velocities, and attenuations) to reservoir properties (double porosities, fluid types, and other thermophysical properties). We consider thermal-induced variations in pore structures and associated effects on the seismic response. The model has the potential to enable seismic rock-physics inversions to estimate the microcrack porosities of existing thermal reservoirs (including the development of microcracks due to the change of heat sources and heating- and cooling-shock effects), to predict the increased microcrack porosity induced by hydraulic fracturing in the EGS, and to identify the fluid type (water or steam) due to the joint effect of pressure and temperature in different depths of thermal reservoirs. Seismic monitoring of thermal memory retention and fading of rocks also is important for sustainable thermal recovery where microcracks could be reduced due to long thermal and pressure treatment in the cyclic recovery. Therefore, the proposed THM model lays the foundation for active (or passive) seismic monitoring of the cyclic recovery of thermal reservoirs.

This paper is organized as follows. First, we briefly introduce the DPT model, followed by a plane-wave analysis to obtain the phase velocity and quality factor of elastic waves. We then formulate the THM thermoelastic model with heating-cooling cycles for a water-saturated granite. Finally, we use the THM thermoelastic model to interpret ultrasonic measurements on granite subject to water-cooling conditions (Shi et al., 2020), where the velocity of elastic waves follows the Kaiser effect due to extensive thermal microcracking during the first thermal cycle. The increased number of thermal cycles does not contribute to the development of more microcracks unless a higher temperature is applied.

DPT MODEL

The DPT model proposed by Li et al. (2022) extends the Lord-Shulman thermo-poroelasticity (Carcione et al., 2019; Wei et al., 2020) to include the double-porosity microstructure, which considers the thermal effects of the fluids, frame, and also their mutual interactions. It should be noted that the dual pores refer to the base (host) pores and microcracks. Such microcracks are compliant pores, including protogenetic, thermal-induced, or hydrofracturing pores. The thermal-cycle system of fracture networks assumes that most microcracks are connected to achieve operational efficiency in the cyclic recovery of thermal reservoirs.

Governing equations

The strain components and stress-strain relations of the solid and fluid are

$$e_{ij} = \frac{1}{2}\left(\partial_j u_i + \partial_i u_j\right)\delta_{ij}, \quad \xi_{ij}^{(m)} = \frac{1}{2}\left(\partial_j U_i^{(m)} + \partial_i U_j^{(m)}\right)\delta_{ij},$$
$$e = e_{ii} = \partial_i u_i, \qquad \xi_m = \xi_{ii}^{(m)} = \partial_i U_i^{(m)}, \tag{1}$$

and

$$\sigma_{ij} = \left(Ae + \sum_m Q_m \xi_m - (\beta - \beta_f)T\right)\delta_{ij} + 2\mu e_{ij},$$
$$\tau^{(m)} = Q_m e + R_m \xi_m - \beta_f T, \tag{2}$$

where e_{ij} ($i, j = 1, 2, 3$), u_i is the strain and displacement components of the solid, $\xi_{ij}^{(m)}$ ($i, j = 1, 2, 3; m = 1, 2$), and $U_i^{(m)}$ ($m = 1, 2$) is the strain and displacement components of the fluid in a double-porosity system. The superscripts $m = 1$ and $m = 2$ represent the host medium and inclusions, respectively. Parameter T is the increment of temperature above a reference absolute temperature T_0 for the state of zero stress and strain. The stiffness coefficients (A, Q_1, Q_2, R_1, R_2, β_f, and β) are given in Appendix A.

Carcione et al. (2019) formulate a modified Fourier law of heat conduction with a relaxation term τ_0 to avoid nonphysical solutions related to classical law. The modified equation for single-porosity media is

$$k\Delta T = \rho c_e(\dot{T} + \tau_0\ddot{T}) + T_0\beta(\dot{e} + \tau_0\ddot{e} + \dot{w}_{i,i} + \tau_0\ddot{w}_{i,i}) + q, \tag{3}$$

where k is the thermal conductivity, Δ is the Laplacian, and c_e is the specific heat capacity. Equation 3 illustrates the coupling between the temperature and THM properties in a single-pore system. An overdot denotes time differentiation and a subindex ",i" denotes a spatial derivative.

However, in a geothermal reservoir, there are two types of pores, i.e., stiff pores and cracks with distinct mechanical properties. Li et al. (2022) define these two types of pore systems with dissimilar porosity values ϕ_{m0} and volume fractions v_m. Equation 3 is generalized to the double-porosity case as follows:

$$k\Delta T = \rho C_e(\dot{T} + \tau_0\ddot{T}) + T_0\beta\left[\dot{e} + \tau_0\ddot{e} + \sum_m (\dot{w}_{i,i}^{(m)} + \tau_0\ddot{w}_{i,i}^{(m)})\right] + q. \tag{4}$$

The filtration of the fluid in the pore system m (Biot, 1962) is $w_i^{(m)} = \phi_m(U_i^{(m)} - u_i)$ and $\phi_m = v_m\phi_{m0}$ denotes the porosities of the host medium ($m = 1$) and inclusions ($m = 2$).

The fluid variation ς represents the LFF, and it satisfies the conservation of fluid mass $\phi_1(\phi_2\varsigma) + \phi_2(-\phi_1\varsigma) = 0$ (Ba et al., 2011). When $v_2 = 0$, this equation yields the modified Fourier law 3.

Finally, the nonisothermal wave equations for double-porosity media saturated with a viscous fluid are (Li et al., 2022)

$$\mu u_{i,jj} + (A+\mu)u_{j,ij} + Q_1\left(U_{j,ij}^{(1)} + \phi_2\varsigma_{,i}\right) + Q_2\left(U_{j,ij}^{(2)} - \phi_1\varsigma_{,i}\right)$$
$$+ (\beta - \beta_f)T_{,i} = \rho_{00}\ddot{u}_i + \sum_m\left[\rho_{0m}\ddot{U}_i^{(m)} + b_m\left(\dot{u}_i - \dot{U}_i^{(m)}\right)\right],$$

$$Q_1 u_{j,ij} + R_1\left(U_{j,ij}^{(1)} + \phi_2\varsigma_{,i}\right) + \frac{\phi_1}{\phi}\beta_f T_{,i} = \rho_{01}\ddot{u}_i + \rho_{11}\ddot{U}_i^{(1)} - b_1\left(\dot{u}_i - \dot{U}_i^{(1)}\right),$$

$$Q_2 u_{j,ij} + R_2(U_{i,ij}^{(2)} - \phi_1\varsigma_{,i}) + \frac{\phi_2}{\phi}\beta_f T_{,i} = \rho_{02}\ddot{u}_i + \rho_{22}\ddot{U}_i^{(2)} - b_2\left(\dot{u}_i - \dot{U}_i^{(2)}\right),$$

$$kT_{,ii} = \rho c_e(\dot{T} + \tau_0\ddot{T}) + T_0\beta\left[(1-\phi)(\dot{u}_{i,i} + \tau_0\ddot{u}_{i,i}) + \sum_m\phi_m\left(\dot{U}_{i,i}^{(m)} + \tau_0\ddot{U}_{i,i}^{(m)}\right)\right],$$

$$\phi_2\left[Q_1 u_{i,i} + R_1\left(U_{i,i}^{(1)} + \phi_2\varsigma_{,i}\right)\right] - \phi_1\left[Q_2 u_{i,i} + R_2\left(U_{i,i}^{(2)} - \phi_1\varsigma_{,i}\right)\right]$$
$$= \frac{1}{3}R_0^2\phi_1^2\phi_{20}\left(-\frac{\rho_f}{\phi_{10}}\ddot{\varsigma}_{,i} + \frac{\eta}{\chi_1}\dot{\varsigma}_{,i}\right), \tag{5}$$

where η and χ_m represent fluid viscosity and skeleton permeability, respectively. The other properties such as density coefficients (ρ_{00}, ρ_{0m}, and ρ_{mm}) and Darcy friction coefficients b_m are given in Appendix A.

Plane-wave analysis

We consider the following plane waves:

$$u_i = Bs_i e^{i\omega(t-\frac{l_j}{v_c}x_j)},$$
$$U_i^{(m)} = C_m d_i e^{i\omega(t-\frac{l_j}{v_c}x_j)},$$
$$T = D e^{i\omega(t-\frac{l_j}{v_c}x_j)},$$
$$\varsigma = E e^{i\omega(t-\frac{l_j}{v_c}x_j)}, \tag{6}$$

where s_i and d_i are the polarizations of the solid and fluid particles, respectively; B, C_m, D, and E are amplitudes; ω is the angular frequency; t is the time; v_c is the complex velocity; l_j and x_j denote the wave directions and the position component, respectively; and $i = \sqrt{-1}$.

Substituting equation 6 into equation 5, we obtain a quadratic equation for the P waves and one solution for the S wave. The solutions yield the frequency-dependent complex phase velocity v_c (see Appendix B).

Following Carcione (2022), the phase velocity, attenuation factor, quality factor, and attenuation coefficient are, respectively,

$$V_P = [\text{Re}(\frac{1}{v_c})]^{-1},$$
$$\alpha = -\omega\text{Im}(\frac{1}{v_c}),$$
$$Q = \frac{\text{Re}(v_c^2)}{\text{Im}(v_c^2)},$$
$$L = 4\pi \cdot \frac{\alpha V_P}{\omega}. \tag{7}$$

MODEL FOR WATER-SATURATED GRANITE

Reservoir rocks experiencing a cold-shock treatment by water-cooling cycles cannot be adequately described by the thermo-mechanical behavior of dry rocks. To include the effect of water-cooling and temperature on the EGS of granite reservoirs, the average THM properties of saturated granite as a function of temperature are collected without losing generality. Such properties are then used in the DPT theory to predict the effect on elastic wave propagation.

THM properties

There are many empirical relations for granite that are derived from extensive analysis of existing data in the literature. In this section, we investigate the temperature-dependent properties of water-saturated granite. Table 1 lists the physical properties of relevant minerals, taken from Mavko and Mukerji (1998).

Thermal conductivity

The empirical thermal conductivity k_m of the dry rock can be derived from (Wang and Konietzky, 2019)

$$k_m/k_{m0} = -5.8126 + 6.8485 \times 0.9995^{T_1} + 0.002172 T_1, \quad 0°C \leq T_1 \leq 1200°C, \quad (8)$$

where k_{m0} is a reference thermal conductivity at room temperature. In a composite rock with grains arranged with a parallel orientation to the direction of heat flow, we have (equation 1 in Robertson [1988])

$$k_{m0} = \sum_i k_i f_i, \quad (9)$$

where k_i is the thermal conductivity of the ith component of the rock shown in Table 1 and f_i is the corresponding volume fraction.

Equation 8 indicates that thermal conductivity is mainly affected by two important factors: mineralogical composition and temperature. The existing equation assumes no change in matrix properties. However, laboratory measurements show significant variations in thermal conductivity for different porosities under dry- and water-saturated conditions (Pai et al., 2021; Ye et al., 2022). Therefore, the combined effect of porosity and pore fluid on thermal conductivity should be considered.

Considering the water properties as a function of pressure and temperature, we analyze the different phases (vapor, liquid, and supercritical) of water in the range of 20°C–400°C and 0–200 MPa. The relevant data are from the fluid thermophysical database provided on the website of the National Institute of Standards and Technology (NIST), which are collected from laboratory measurements by Lemmon et al. (2005). The pressure and temperature dependence of water are shown in Figures 1a and 2a. We see that water boils at the standard ambient pressure: $P = 0.1013$ MPa and $T_1 = 99.8°C$. At higher temperatures, water and steam coexist at the equilibrium determined by the vapor-pressure curve that ends at the critical point (Johnston and Penninger, 1989). The inflection point, beyond which water changes its properties rapidly, is defined as the supercritical point that occurs at $P = 22.06$ MPa and $T_1 = 373.9°C$, associated with an abrupt change of equivalent properties in the saturated rock, as shown in Figures 1 and 2.

For the water-saturated granite, the effective thermal conductivity is (Albert et al., 2017)

$$k_{\text{effect}} = k_m \cdot \left(\frac{1 - \phi}{1 + \phi}\right)^a + k_{\text{water}} \phi^b, \quad 0°C \leq T_1 \leq 1200°C, \quad (10)$$

where a and b are fitting parameters and ϕ is the total porosity. Here, we set $a = 1.08$ and $b = 0.4$.

Figure 1b shows the thermal conductivity of water-saturated granite as a function of P, T_1, and ϕ, based on the empirical relations 8 and 10. The equivalent thermal conductivity k_{effect} generally decreases with increasing temperature and decreasing pressure and porosity due to the temperature-dependent thermal conductivity of dry rock matrix k_m (see equation 8). As shown in equation 10, pore structures and fluid properties also affect k_{effect}. As a whole, k_{effect} tends to increase with increasing pressure and decreasing porosity. It is worth noting that the thermal conductivity of water shows obvious decreases in a relatively broad region around the critical point, as shown in Figure 1a. These changes in the water state are responsible for the alteration of the equivalent thermal conductivity k_{effect}. For instance, water cooling often reduces the effective thermal conductivity of saturated rocks. The thermal conductivity varies with T_1 and P, which is more obvious for water-saturated rocks than in the dry condition, as shown in Figure 1b for k_m (the pink plane). This is because the influence of cold shocks by injected cold water is more significant than that of slow cooling (air cooling) on rock failure (Kumari et al., 2017), causing fracture growth with a higher ϕ, and hence a greater k_{effect}.

Specific heat

Wang and Konietzky (2019) indicate that the specific heat shows a sudden drop when temperature T_1 reaches 600°C, which could be caused by the phase transition of quartz ($T_{\alpha-\beta} = 573°C$; Lindroth and Krawza, 1971). The empirical specific heat capacity c_m of the dry rock can be described as

Table 1. Physical properties of the minerals.

Group	Mineral	α_t[4] (10^{-6}/K)	k[4] (m·kg/[s^3·K])	c_m[4] (m^2/[s^2·K])	K[5] (GPa)	G[5] (GPa)	Pct (%)
Quartz	Quartz	13.4	7.7	750	37	44	11.89
Feldspar	"Average" feldspar	3.65	2.165	712	37.5	15	72.21
Mica	Biotite	12.81	2.01	770	50.4	27.35	15.9

Note: α_t, coefficient of thermal expansion; k, thermal conductivity; c_m, specific heat; K, bulk modulus; G, shear modulus; Pct, the volume fraction of minerals in granite.
[4]Data from Wang and Konietzky (2022).
[5]Data from Mavko et al. (2003).

$$\frac{c_m}{c_{m0}} = 0.957 + 6.59 \times 10^{-4} T_1, \quad 0°C \leq T_1 \leq 575°C, \quad (11)$$

where c_{m0} is the corresponding initial value at room temperature defined as (equation 14 in Robertson [1988])

$$c_{m0} = \sum_i c_i f_i, \quad (12)$$

where c_i is the specific heat of the ith component of the rock shown in Table 1 and f_i is the corresponding volume fraction.

Based on the physical properties of relevant minerals listed in Table 1, we calculate the effective specific heat of water-saturated rocks (Sultan et al., 2004):

$$c_{effect} = c_m \cdot \frac{(1 - \phi) \cdot \rho_{rock}}{\rho_{effect}} + c_{water} \cdot \frac{\phi \cdot \rho_{water}}{\rho_{effect}}. \quad (13)$$

The results are shown in Figure 2b as a function of pressure and temperature. We see that dramatic changes in c_{effect} occur near the critical point due to the supercritical pore-fluid properties.
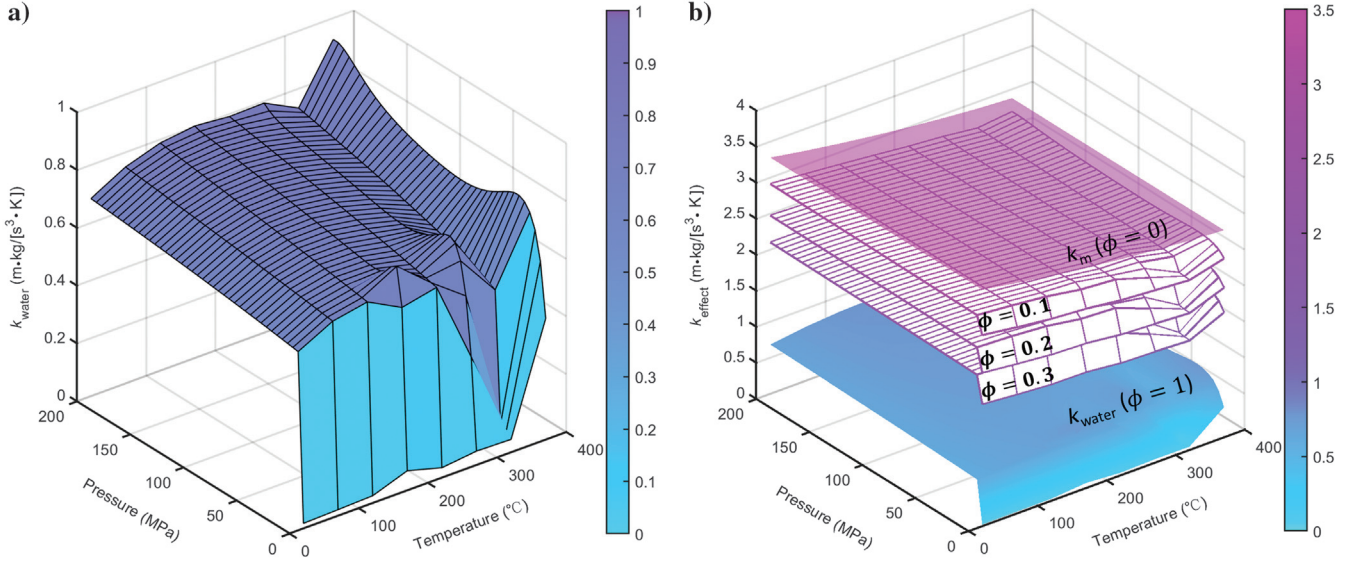
Figure 1. Effective thermal conductivity of water and granite as a function of pressure (P) and temperature (T_1) for different porosities. (a) Water thermal conductivity for a wide range of pressure and temperature (data from the NIST website) and (b) upper limit controlled by different initial values (dry granite) and lower limit controlled by fluid (water).
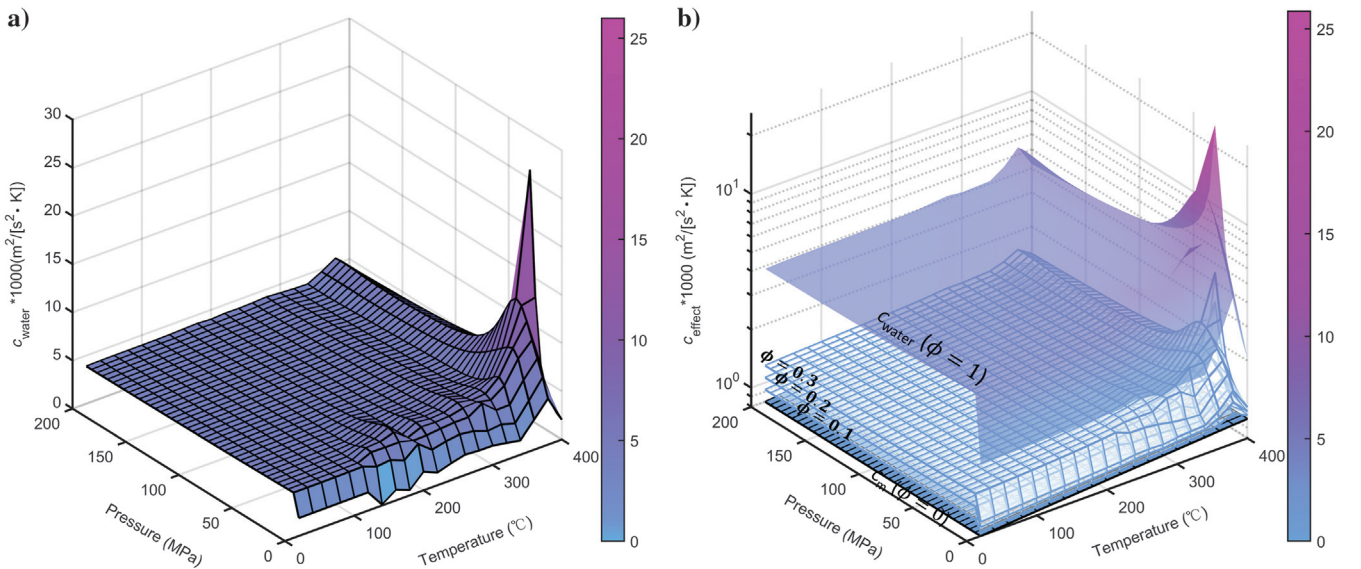

Figure 2. (a) Pressure- and temperature-dependent water-specific heat (data from the NIST website) and (b) effective specific heat of the water-saturated granite with the upper limit controlled by water and the lower limit controlled by dry granite for different porosities.

Moreover, c_{effect} changes between c_m and c_{water}, and approaches to specific heat of water with increasing porosity (fluid content).

Crack porosity

It is well known that the P-wave velocity is sensitive to the presence of (micro)cracks (e.g., Ayling et al., 1995; Ba et al., 2011; Li et al., 2021). The crack density increases in granite greater than 100°C–120°C (Lin, 2002; Junique et al., 2021). Thermally induced inter- and intragranular cracks play a predominant role, with (1) the mismatch of the coefficients of thermal expansion between adjacent grains (intergranular crack; Wang and Konietzky, 2022) and (2) loss of the fluid inclusions and interlayer bound water. The osmotic effect and hydration of minerals limit the impact on the boundary and intergranular crack (Wang et al., 2014). Some experiments indicate that 400°C may be a threshold temperature at which granite generates numerous microcracks (Chaki et al., 2008; Shi et al., 2020).

Yang et al. (2022b) state that, to evaluate the crack porosity from the measurements, it is necessary to link the 2D (length and width) to the 3D (volume density) crack features. Based on the assumption of isotropy, the crack porosity (ϕ_{20}) can be estimated from 2D measurements by

$$\phi_{20} = \frac{4\pi W_a l^2}{3}\Gamma_{\text{crack}}, \tag{14}$$

where W_a, l, and Γ_{crack} are the average width, length, and plane density of cracks, respectively.

Homand-Etienne and Houpert (1989) present an empirical law for the normalized coefficient ϕ_2/ϕ_{20} of granites. Figure 3a shows that, below 500°C, this specific value for the different granites (color dots) increases exponentially with the temperature, with the distribution of data points being dispersed greater than 500°C because of the phase transition of quartz and the further increase in crack density. By fitting the data collected from the different sources (e.g., Homand-Etienne and Houpert, 1989; Tian et al., 2021), an empirical relation between the temperature and crack porosity is obtained (the dashed line in Figure 3a) as

$$\phi_2/\phi_{20} = 0.8376e^{0.0054T_1}, \ 20°C \leq T_1 \leq 600°C. \tag{15}$$

Figure 3b and 3c displays the host porosity as a function of thermal cycles and temperature, respectively. It should be stressed that the porosity reported by Shi et al. (2020) is measured at a hydrostatic pressure of 3.5 MPa under the assumption that the crack porosity is constant below a certain confining pressure that is used only to maintain the rock integrity at high temperatures. Two distinct stages are identified in Figure 3c: from 200°C to 400°C (stage 1) where ϕ_1 is almost constant and from 400°C to 600°C (stage 2) where the porosity increases abruptly.

Workflow of the model

Figure 4 shows a workflow to estimate the pressure- and temperature-dependent P-wave velocity for a water-saturated granite during the cooling-heating cycles. There are three major steps to determine the pressure- and temperature-dependent fluid properties, temperature-dependent skeleton properties, and double-porosity geometries.

First, we assume that ϕ_1 is constant and $\phi_2(T)$ depends on the temperature of the initial granite porosity (see Table 2) at room temperature. The effective grain bulk and shear moduli (K_s and μ_s) are determined from mineral percentages (see Table 1) by using the Voigt–Reuss–Hill average. Based on the empirical equation (Ba et al., 2011) used to obtain the dry-rock bulk and shear moduli (K_b and μ_b), the moduli of the two phases are

$$K_{bm} = (1 - \phi_m)K_s/(1 + C_m\phi_m),$$
$$1/K_b = v_1/K_{b1} + v_2/K_{b2},$$
$$\mu_b = (1 - \phi)\mu_s/(1 - C_s\phi), \tag{16}$$

where C_m is the bulk consolidation coefficients and C_s is the shear consolidation coefficient.

Figure 5 shows the dry-rock moduli as a function of crack porosities for different consolidation coefficients. In general, the moduli decrease with increasing crack and stiff (host) porosities.

We consider pressure- and temperature-dependent fluid properties, as shown in Figures 1 and 2. Table 2 shows the initial properties of granite and pure water at room temperature (25°C). From equations 8 to 15, we obtain the THM properties of water-saturated granite at different temperatures, where the quantities $k_{\text{effect}}(P, T_1)$, c_{effect}
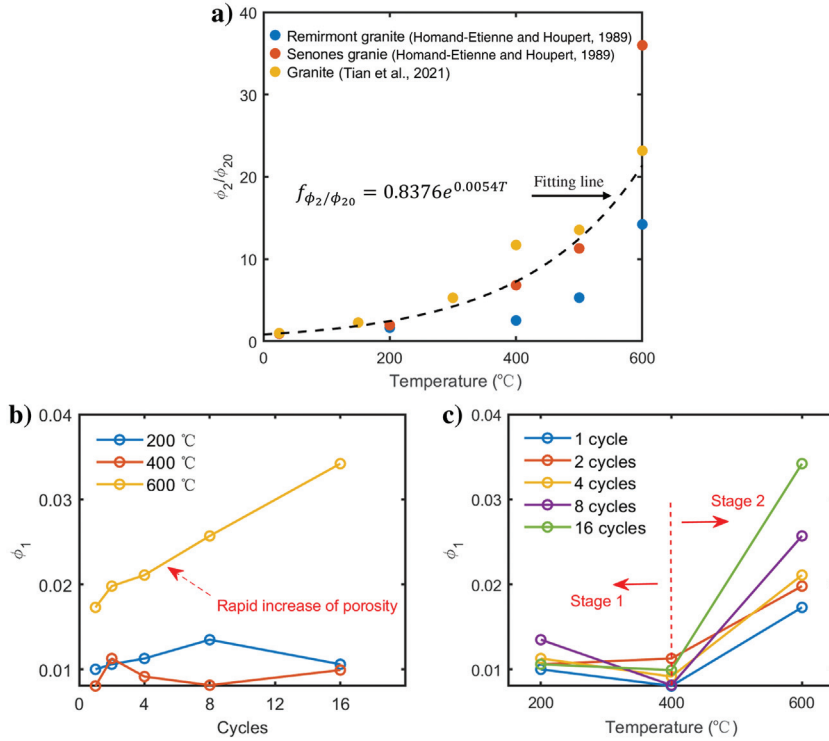
Figure 3. Thermal effects on the porosity of granite: (a) temperature-dependent crack porosity, (b) host porosity during the thermal cycles, and (c) temperature-dependent host porosity (modified from Shi et al., 2020).

(P, T_1), and $\phi_2(T_1)$ are temperature dependent. Based on these temperature-dependent properties, we calculate the P-wave velocity and attenuation of saturated granites at different temperatures and frequencies from the equations given in Appendix B.

Velocity-temperature relation for saturated granites

Sensitivity analysis

We calculate the P-wave velocity variation with temperature for three sets of parameters. Figure 6 compares temperature-dependent P-wave velocities induced by different THM properties for two cases in each set: (1) the THM properties are independent of the temperature (indicated by the black lines), i.e., the temperature only appears in the DPT model and (2) the effect of the temperature is fully considered (indicated by the blue lines).

From Figure 6, we see that the P-wave velocities show little change with the thermal conductivity (k_{effect}) and specific heat (c_{effect}) in the pressure-temperature range studied, whereas the temperature-dependent crack porosity (ϕ_2) significantly affects the P-wave velocity.

Application

We consider the granite from Zhangzhou, Fujian. Shi et al. (2020) measure the P-wave velocities at six different temperatures (from 20℃ to 600℃) after cooling by water to model the high-temperature condition of deep bedrocks in an EGS system. The samples are composed of quartz, anorthite, and biotite with a small amount of pyroxene and magnetite. The host and crack porosities can be estimated from polarized micrographs as 1.73% and 0.04%, respectively, at room temperature without thermal treatments. Cracks develop with increasing temperature, observed from plane-polarized and cross-polarized cast thin section images. We use a least-squares regression to fit the volume fraction of cumulative cracks at each temperature, where the initial volume ratios of the two types of pores are $v_1 = 0.985$ and $v_2 = 0.015$, respectively.

Based on the relevant physical properties shown in Tables 1 and 3, we estimate the temperature-dependent P-wave velocities. Figure 7 compares the result to the measurements by water-cooling (the red dots). We see that the nonlinear curve can roughly be divided into two parts with an inflection point at 200℃. In the first part (T_1 = 20℃–200℃), a relatively rapid drop in velocity below 100℃ corresponds to the evaporation of adsorbed and interlayer water, which tends to cause the closure of microstructures and increases the strength of the cement (Sun et al., 2013). Then, the cementation effect partly inhibits the thermal expansion stress (Li et al., 2021). Therefore, the resulting overall variation is rather gentle. In the second part (T_1 = 200℃–400℃), we see a rapid decrease due to the exponential growth in crack porosity, where the effects of thermal conductivity and specific heat are not significant (Zhang et al., 2018). Following the workflow described previously (see Figure 7), the theoretical P-wave velocity is overall consistent with the data, implying that the DPT model and temperature-dependent critical properties can describe the P-wave velocity variations under heating

and water cooling. Beyond 400℃, there are plastic deformations that cannot be modeled with the THM thermoelastic theory. Moreover, the temperature cycles may cause irreversible damage to the rock and eventually lead to a temperature-independent micropore structure after repeated water cooling (Wang et al., 2014). Scarce experimental data limit our investigations on this issue.

RESULTS FOR WATER-SATURATED GRANITE

We take the water-saturated granite at 300℃ as an example, where the phase velocity and attenuation are calculated as a function of frequency for different values of the THM properties (thermal conductivity, specific heat, and crack porosity) (see Table 3). Here, we attempt small specific heats to highlight the thermal effect on the thermoelastic properties of saturated porous media (Carcione et al., 2019; Wei et al., 2020).

Figure 8 shows the frequency-dependent phase velocities and attenuation coefficients of the fast P, slow P1, slow P2, and thermal P waves for the water-saturated granite with the relevant properties listed in Table 3 where the thermal conductivities vary as indicated in Figure 8. We see that the fast P velocity has two inflection points (Figure 8a), corresponding to two attenuation peaks (Figure 8b). The stronger peak appears at the low frequencies (10^2–10^3 Hz), corresponding to the mesoscopic energy loss caused by LFF. The relaxation peak at the ultrasonic frequencies corresponds to the Biot mechanism (Biot, 1962) that describes the friction dissipation due to the filtration of pore fluids under seismic wave excitation. The fast P, slow P2 (Biot), and thermal P velocities as well as the LFF and Biot attenuation peaks (Figure 8b) hardly vary with the thermal
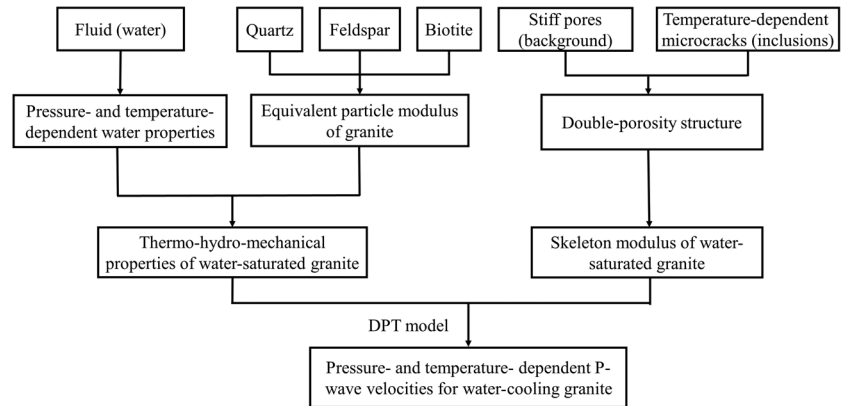
Figure 4. Workflow for the THM thermoelastic model applied to laboratory and log data.

Table 2. Physical properties of grains and water.

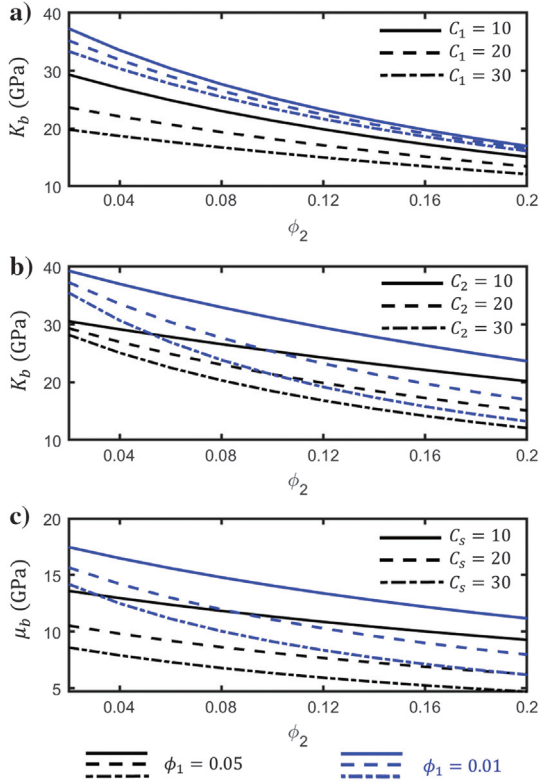| Property	Initial value
Grain bulk modulus (K_s)	45 GPa
Shear modulus (μ_s)	20 GPa
Volume fraction of pore 1 (v_1)	0.7
Volume fraction of pore 2 (v_2)	0.3
Fluid density (ρ_f)	1000 kg/m^3
Bulk modulus (K_f)	2.2 GPa

Figure 5. Dry-rock moduli as a function of crack porosities in granite with the different (a) host (bulk), (b) crack (bulk), and (c) shear consolidation coefficients. The black and blue lines refer to host porosities of 0.05 and 0.01, respectively.
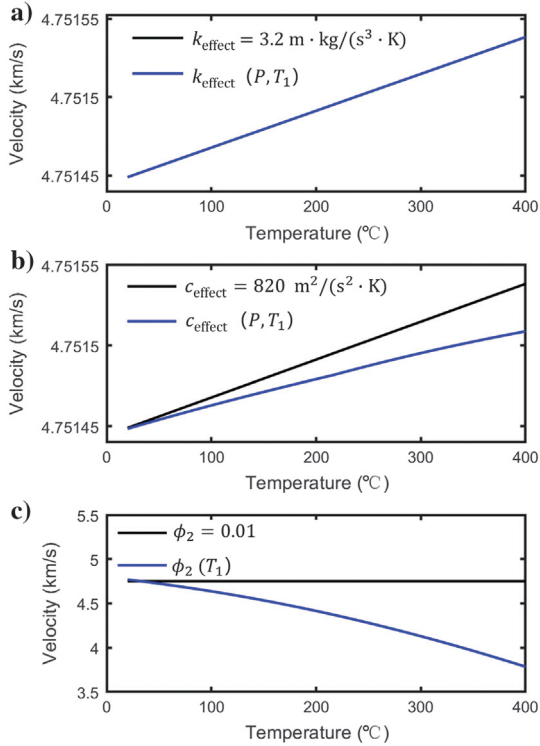

Figure 6. Comparison of temperature-dependent P-wave velocities induced by the different THM properties: (a) thermal conductivity, (b) specific heat, and (c) crack porosity.

conductivities (Figure 8a, 8e, and 8g). Figure 8c shows that the slow P1 velocity increases significantly with increasing thermal conductivities, with the relative change rate of 11.7% much larger than 1.8% of the fast P velocity. This implies that the host porosity plays

Table 3. Physical properties of water-saturated granite.

| Property	Value
Grain bulk modulus (K_s)	44 GPa
Shear modulus (μ_s)	24 GPa
Density (ρ_s)	2650 kg/m^3
Frame porosity of pore 1 (ϕ_1)	1.73%
Consolidation parameters (C_1)	10
Permeability of pore 1 (χ_1)	4×10^{-4} mD
Porosity of pore 2 (ϕ_2)	0.04%
Consolidation parameters (C_2)	200
Permeability of pore 2 (χ_2)	20 mD
Fluid density (ρ_f)	1000 kg/m^3
Bulk modulus (K_f)	2.2 GPa
Viscosity (η)	0.001 Pa s
Thermoelasticity coefficient (β_f)	40,000 kg/(m·s^2·K)
Thermal conductivity (k_f)	0.6 m·kg/(s^3·K)
Bulk specific heat capacity (c_{m0})	820 m^2/(s^2·K)
Thermoelasticity coefficient (β)	112,000 kg/(m·s^2·K)
Absolute temperature (T_0)	300 K
Thermal conductivity (k_0)	3.2 m·kg/(s^3·K)
Relaxation time (τ_0)	1.5×10^{-8} s
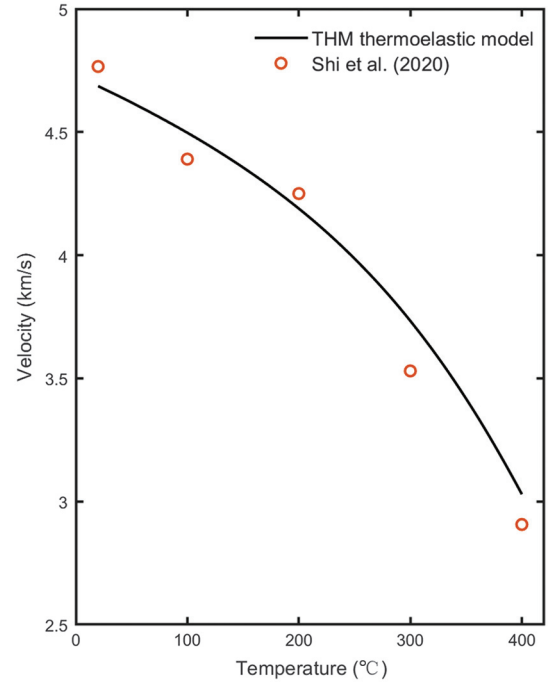
Figure 7. Predicted and measured ultrasonic P-wave velocity as a function of temperature.

an important part in enhancing thermal recovery. Because the thermal conductivity of a saturated rock consists of double-pore phases (see equation 10), we further investigate the dependence of the slow P1 velocity on the fluid thermal conductivity. Figure 9a displays that this slow P1 velocity is hardly affected by the fluid thermal conductivity that can be ignored. However, Figures 8 and 9 illustrate that the increase in phase velocities only occurs in the ultrasonic frequency band (greater than 10^7 Hz). The thermal peak is additional energy dissipation caused by mode conversion, similar to the wave-induced fluid-flow attenuation in poroelasticity. On the seismic frequency band, the Biot and thermal peaks are much smaller if homogeneous media are considered.

Figure 10 shows the frequency-dependent phase velocities and attenuation coefficients of the four longitudinal waves for the water-saturated granite with different specific heats marked. We see that the fast P velocity (Figure 10a) significantly decreases with the increasing specific heat. The resulting attenuation (Figure 10b) presents three inflection points that correspond to the LFF, Biot, and thermal attenuation peaks, respectively. The slow P1 velocity (Figure 10c) shows some changes with specific heats, whereas the slow P2 (Figure 10e) and thermal P (Figure 10g) velocities are almost constant with specific heats. Therefore, specific heat is impor-

tant for improving the production performance of EGS. Figure 11 indicates that the effect of fluid-specific heats can be negligible on the slow P1 velocity.

Figure 12 shows the frequency-dependent phase velocities and attenuation coefficients of the four longitudinal waves for the water-saturated granite with different host porosities. As expected, the fast P velocity (Figure 12a) significantly decreases with increasing

Figure 9. (a) Phase velocity and (b) attenuation coefficient of the slow P1 wave as a function of frequency for different fluid thermal conductivities.
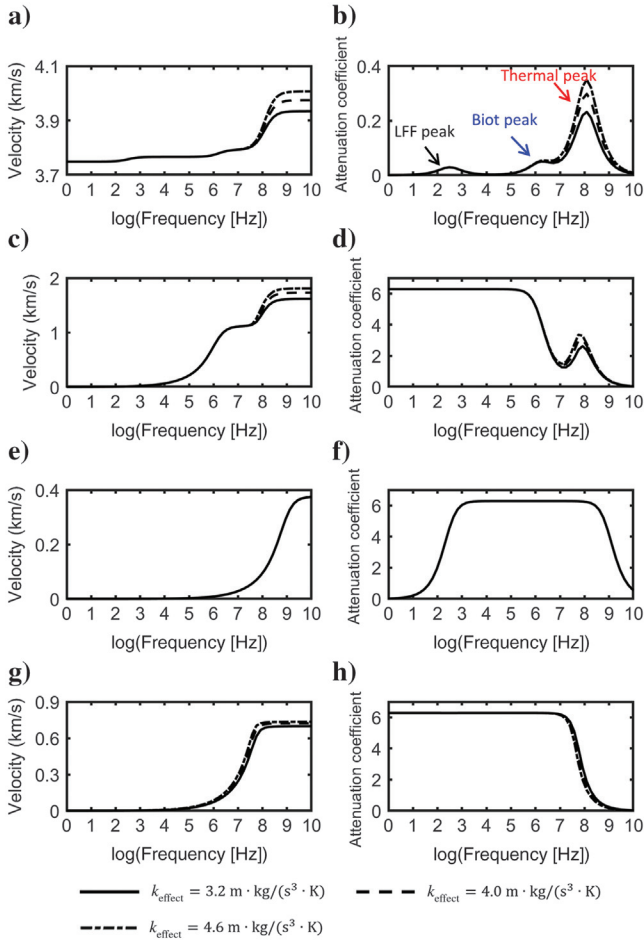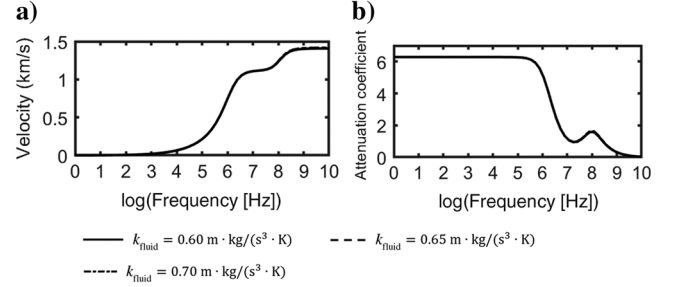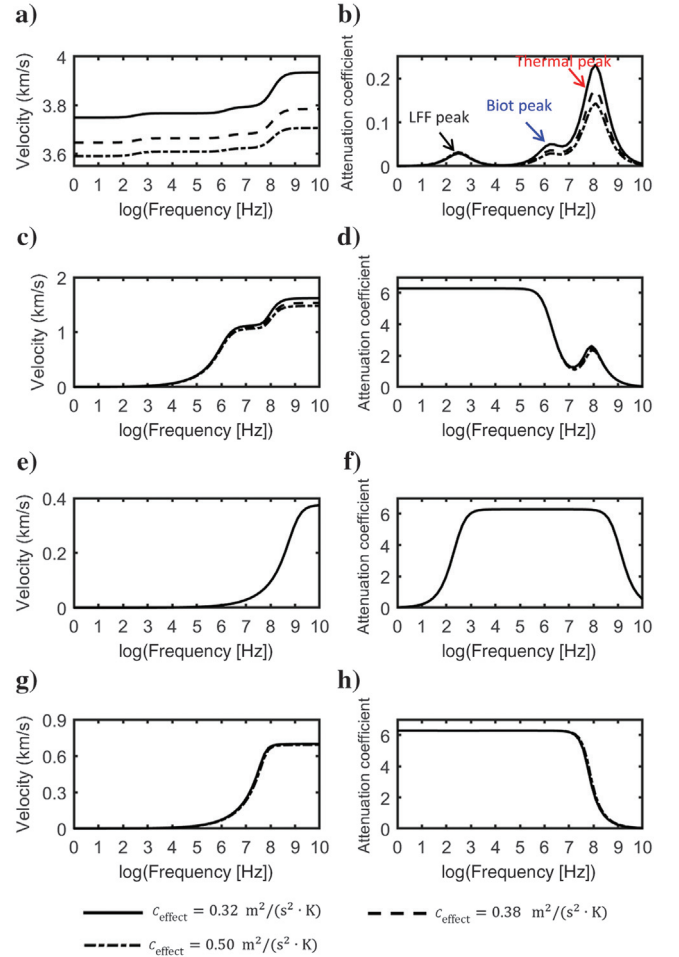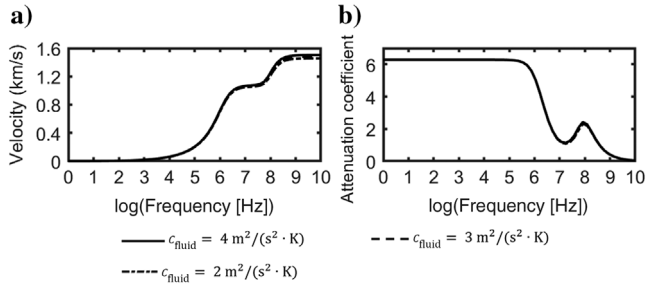
Figure 8. (a, c, e, and g) Frequency-dependent phase velocity and (b, d, f, and h) attenuation coefficient of the (a and b) fast P, (c and d) slow P1, (e and f) slow P2, and (g and h) thermal P waves for different thermal conductivities. The properties are listed in Table 3.
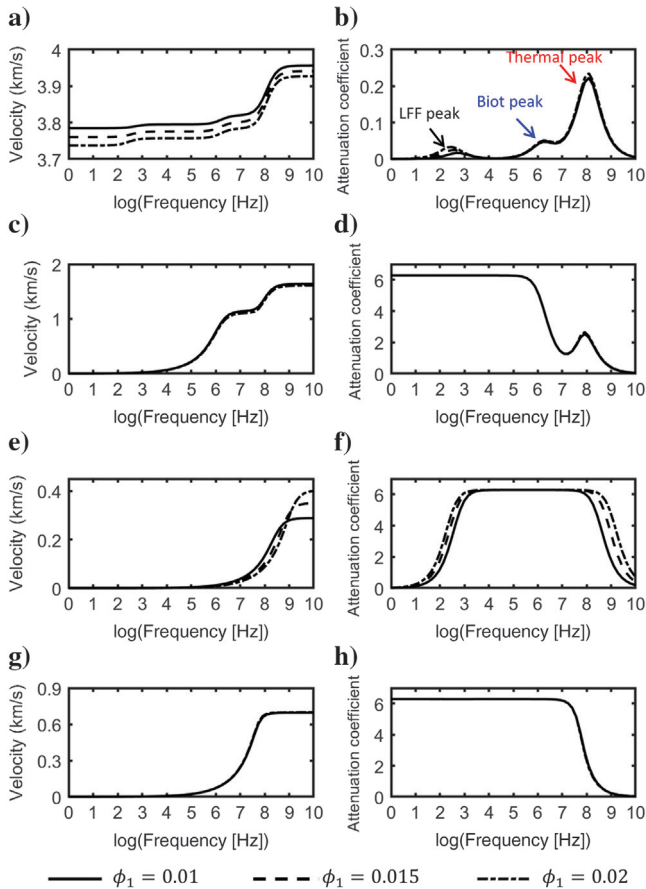
Figure 10. (a, c, e, and g) Frequency-dependent phase velocity and (b, d, f, and h) attenuation coefficient of the (a and b) fast P, (c and d) slow P1, (e and f) slow P2, and (g and h) thermal P waves for different specific heats. The properties are listed in Table 3.

porosities because of decreasing frame moduli. The resulting attenuation (Figure 12b) has three peaks corresponding to the mesoscopic energy loss (10^2–10^3 Hz), the Biot mechanism (Biot, 1962) (10^6–10^7 Hz), and the thermal attenuation at approximately 10^8 Hz, respectively. The velocity and attenuation of slow P1 and slow P2 waves are hardly affected by the host porosity below 10^7 Hz, as well as the thermal P-wave velocity (Figure 12g and 12h). Comparing the effects of host porosities on the heat exchange in the rock matrix (Figure 12a) and host pores (Figure 12c), we

Figure 11. (a) Phase velocity and (b) attenuation coefficient of the slow P1 wave as a function of frequency for different fluid-specific heats.

Figure 12. (a, c, e, and g) Frequency-dependent phase velocity and (b, d, f, and h) attenuation coefficient of the (a and b) fast P, (c and d) slow P1, (e and f) slow P2, and (g and h) thermal P waves for different host porosities. The properties are listed in Table 3.
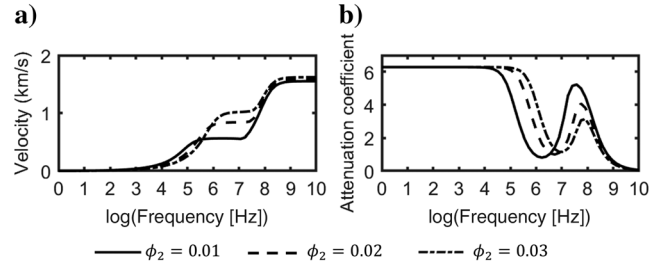

Figure 13. (a) Phase velocity and (b) attenuation coefficient of the slow P1 wave as a function of frequency for different crack porosities.

deduce that the heat extraction process in EGS cannot be improved by increasing host porosities.

Finally, Figure 13 shows the frequency-dependent slow P1 velocity and attenuation with crack porosities. We see that, between 0.01 and 0.02, the velocity increases in the range of 10^5–10^8 Hz. Improving the connectivity between pore types is better than increasing the stiff porosity to enhance thermal production.

CONCLUSION

Granite thermal reservoirs generally consist of stiff (host) pores and cracks, which provide the main channels for heat exchange and fluid flow. The cyclic recovery of such typical granite reservoirs involves a complex THM coupling process. We apply a DPT theory to the THM coupling process to interpret ultrasonic measurements on granite under water-cooling conditions by assuming that cracks/fractures are embedded in an isotropic porous medium.

A plane-wave analysis for the water-saturated granite reveals the presence of the classical P and S waves and three slow P waves, namely the slow P1 (Biot), the slow P2 (Biot), and a thermal P. The frequency- and temperature-dependent behaviors of these slow waves show that the thermal conductivity and specific heat affect the relaxation peaks, related to the mesoscopic and Biot loss mechanisms. These thermoelastic properties have negligible effects in the seismic band for the temperature range of less than 400°C. The host (stiff) porosity mainly affects the mesoscopic loss with little influence on the Biot loss, whereas the soft crack/fracture porosity becomes important in low frequencies. The proposed THM thermoelastic model attempts to bridge thermoelastic parameters (moduli, velocities, and attenuations) and reservoir properties (double porosities and fluid type). It describes dramatic velocity changes due to thermal-induced microcracking during the heating process (particularly in the first cycle). The THM model has the potential to enable seismic rock-physics inversions to estimate the crack porosities of thermal reservoirs (including the development of microcracks induced by heating- and cooling-shock effects and hydraulic fracturing in the EGS) and to identify the fluid type (water or steam) due to the joint effect of pressure and temperature in the different depths of thermal reservoirs.

Oil & Gas Geophysical Exploration" (B18055). The authors thank editor E. Gasperikova and anonymous reviewers for their constructive comments and suggestions.

DATA AND MATERIALS AVAILABILITY

Data associated with this research are available and can be obtained by contacting the corresponding author.

APPENDIX A

STIFFNESS COEFFICIENTS OF THE BIOT-RAYLEIGH THEORY

The stiffness coefficients of the Biot-Rayleigh theory are (Ba et al., 2011)

$$
\begin{aligned}
Q_1 &= \frac{\alpha^*(1-\phi-K_b/K_s)\phi_1 K_s}{\alpha^*(1-\phi-\frac{K_b}{K_s})\phi_1 K_s + \frac{K_s(\alpha^*\phi_1+\phi_2)}{K_f}}, \\
Q_2 &= \frac{(1-\phi-K_b/K_s)\phi_2 K_s}{1-\phi-\frac{K_b}{K_s}+\frac{K_s(\alpha^*\phi_1+\phi_2)}{K_f}}, \\
R_1 &= \frac{(\alpha^*\phi_1+\phi_2)\phi_1 K_s}{\alpha^*(1-\phi-\frac{K_b}{K_s})\phi_1 K_s + \frac{K_s(\alpha^*\phi_1+\phi_2)}{K_f}}, \\
R_2 &= \frac{(\alpha^*\phi_1+\phi_2)\phi_2 K_s}{1-\phi-\frac{K_b}{K_s}+\frac{K_s(\alpha^*\phi_1+\phi_2)}{K_f}}, \\
A &= (1-\phi)K_s - \frac{2}{3}\mu - \frac{K_s}{K_f}(Q_1+Q_2), \\
\beta &= \beta_s + (1-\frac{K_b}{K_s})\beta_f,
\end{aligned}
\tag{A-1}
$$

where $\alpha^* = \xi_1/\xi_2$; K_s and K_f are the grain and fluid bulk moduli, respectively; and the dry-rock modulus K_b is obtained from equation 16. Here, β_s and β_f are the coefficients of thermal stress (Carcione et al., 2019) for the solid and fluid, respectively; ϕ_m are the host ($m = 1$) and crack ($m = 2$) porosities; and b_1 and b_2 are dissipation parameters given by

$$
b_m = -\phi_m \phi_{m0} \frac{\eta}{\chi_m}
\tag{A-2}
$$

and the density coefficients are

$$
\begin{aligned}
\rho_{00} &= (1-\phi)\rho_s - \rho_f \sum_m \phi_m(1-\tau_m), \\
\rho_{0m} &= \rho_f \phi_m(1-\tau_m), \\
\rho_{mm} &= \rho_f \phi_m \tau_m, \\
\rho &= (1-\phi)\rho_s + \rho_f \phi,
\end{aligned}
\tag{A-3}
$$

where the total porosity is $\phi = \phi_1 + \phi_2$ and $\phi_m = v_m \phi_{m0}$, with v_m being the volume fraction of phase m and ϕ_{m0} being the porosity in each phase; moreover, $\tau_m = 0.5((1/\phi_m) + 1)$ is the tortuosity.

APPENDIX B

SOLUTIONS OF MOTION EQUATIONS

Substituting a P-wave plane-wave solution into equation 5, we obtain

$$
\begin{vmatrix}
a_{11}v_c^2 + b_{11} & a_{12}v_c^2 + b_{12} & a_{13}v_c^2 + b_{13} & a_{14}v_c \\
a_{21}v_c^2 + b_{21} & a_{22}v_c^2 + b_{22} & a_{23}v_c^2 + b_{23} & a_{24}v_c \\
a_{31}v_c^2 + b_{31} & a_{32}v_c^2 + b_{32} & a_{33}v_c^2 + b_{33} & a_{34}v_c \\
a_{41}v_c & a_{42}v_c & a_{43}v_c & a_{44}v_c^2 + b_{44}
\end{vmatrix} = 0,
\tag{B-1}
$$

where

$$
\begin{aligned}
a_{11} &= (b_1+b_2)i/\omega - \rho_{00}, \\
b_{11} &= [A+2\mu+i(Q_2\phi_1-Q_1\phi_2)x_1]\omega^2, \quad a_{12} = -b_1 i/\omega - \rho_{01}, \\
b_{12} &= [Q_1+i(Q_2\phi_1-Q_1\phi_2)x_2]\omega^2, \quad a_{13} = -b_2 i/\omega - \rho_{02}, \\
b_{13} &= [Q_2+i(Q_2\phi_1-Q_1\phi_2)x_3]\omega^2, \quad a_{14} = -(\beta-\beta_f)i/\omega, \\
a_{21} &= -b_1 i/\omega - \rho_{01}, \quad b_{21} = [Q_1-iR_1\phi_2 x_1]\omega^2, \\
a_{22} &= b_1 i/\omega - \rho_{11}, \quad b_{22} = [R_1-iR_1\phi_2 x_2]\omega^2, \quad a_{23} = 0, \\
b_{23} &= -iR_1\phi_2 x_3\omega^2, \quad a_{24} = -\frac{\phi_1\beta_f i}{\phi\omega}, \quad a_{31} = -b_2 i/\omega - \rho_{02}, \\
b_{31} &= [Q_2+iR_2\phi_1 x_1]\omega^2, \quad a_{32} = 0, \quad b_{32} = iR_2\phi_1 x_2\omega^2, \\
a_{33} &= b_2 i/\omega - \rho_{22}, \quad b_{33} = [R_2+iR_2\phi_1 x_3]\omega^2, \quad a_{34} = -\frac{\phi_2\beta_f i}{\phi\omega}, \\
a_{41} &= T_0\beta(1-\phi)(\tau_0 i\omega^3+\omega^2), \quad a_{42} = T_0\beta\phi_1(\tau_0 i\omega^3+\omega^2), \\
a_{43} &= T_0\beta\phi_2(\tau_0 i\omega^3+\omega^2), \quad a_{44} = \rho c_e(i\omega-\tau_0\omega^2), \\
b_{44} &= k\omega^2,
\end{aligned}
\tag{B-2}
$$

where

$$
\begin{aligned}
x_1 &= i(\phi_2 Q_1 - \phi_1 Q_2)/Z, \quad x_2 = i\phi_2 R_1/Z, \quad x_3 = -i\phi_1 R_2/Z, \\
Z &= -\tfrac{1}{3}\omega\phi_1^2\phi_2\phi_{20}R_0^2(i\eta/\chi_1 + \omega\rho/\phi_{10}) - (\phi_2^2 R_1 + \phi_1^2 R_2).
\end{aligned}
\tag{B-3}
$$

Equation B-1 gives three roots, corresponding to a fast P wave and two slow P waves denoted by P1 and P2.

Similarly, by substituting the plane-wave solution of an S wave into equation 5, we obtain

$$
\mu\left(\frac{1}{v_c}\right)^2 = \rho_{00} - \frac{i(b_1+b_2)}{\omega} - \frac{\left(\rho_{01}+\frac{ib_1}{\omega}\right)^2}{\rho_{11}-\frac{ib_1}{\omega}} - \frac{\left(\rho_{02}+\frac{ib_2}{\omega}\right)^2}{\rho_{22}-\frac{ib_2}{\omega}}.
\tag{B-4}
$$

The S-wave complex velocity is not affected by the thermal properties (in homogeneous media).

REFERENCES

Albert, K., M. Schulze, C. Franz, R. Koenigsdorff, and K. Zosseder, 2017, Thermal conductivity estimation model considering the effect of water saturation explaining the heterogeneity of rock thermal conductivity: Geothermics, **66**, 1–12, doi: 10.1016/j.geothermics.2016.11.006.

Ayling, M. R., P. G. Meredith, and S. A. Murrell, 1995, Microcracking during triaxial deformation of porous rocks monitored by changes in rock physical properties, I. Elastic-wave propagation measurements on dry rocks: Tectonophysics, **245**, 205–221, doi: 10.1016/0040-1951(94)00235-2.

Ba, J., J. M. Carcione, and J. X. Nie, 2011, Biot-Rayleigh theory of wave propagation in double-porosity media: Journal of Geophysical Research: Solid Earth, **116**, doi: 10.1029/2010JB008185.

Batzle, M. L., and Z. Wang, 1992, Seismic properties of pore fluids: Geophysics, **57**, 1396–1408, doi: 10.1190/1.1443207.

Berard, T., and F. H. Cornet, 2003, Evidence of thermally induced borehole elongation: A case study at Soultz, France: International Journal of Rock Mechanics and Mining Sciences, **40**, 1121–1140, doi: 10.1016/S1365-1609(03)00118-7.

Biot, M. A., 1962, Mechanics of deformation and acoustic propagation in porous media: Journal of Applied Physics, **33**, 1482–1498, doi: 10.1063/1.1728759.

Breede, K., K. Dzebisashvili, X. Liu, and G. Falcone, 2013, A systematic review of enhanced (or engineered) geothermal systems: Past, present and future: Geothermal Energy, **1**, 1–27, doi: 10.1186/2195-9706-1-4.

Buijze, L., L. van Bijsterveldt, H. Cremer, B. Paap, H. Veldkamp, B. B. T. Wassing, J. D. Wess, G. C. N. van Yperen, J. H. ten Heege, and B. Jaarsma, 2019, Review of induced seismicity in geothermal systems worldwide and implications for geothermal systems in the Netherlands: Netherlands Journal of Geosciences, 98, doi: 10.1017/njg.2019.6.

Cacace, M., H. Hofmann, and S. A. Shapiro, 2021, Projecting seismicity induced by complex alterations of underground stresses with applications to geothermal systems: Scientific Reports, **11**, 1–10, doi: 10.1038/s41598-021-02857-0.

Carcione, J. M., 2022, Wave fields in real media: Wave propagation in anisotropic, anelastic porous and electromagnetic media, 4th ed.: Elsevier Science.

Carcione, J. M., F. Cavallini, E. Wang, J. Ba, and L. Y. Fu, 2019, Physics and simulation of wave propagation in linear thermoporoelastic media: Journal of Geophysical Research: Solid Earth, **124**, 8147–8166, doi: 10.1029/2019JB017851.

Chaki, S., M. Takarli, and W. P. Agbodjan, 2008, Influence of thermal damage on physical properties of a granite rock: Porosity, permeability and ultrasonic wave evolutions: Construction and Building Materials, **22**, 1456–1461, doi: 10.1016/j.conbuildmat.2007.04.002.

Chen, B. G., E. X. Song, and X. H. Cheng, 2014, A numerical method for discrete fracture network model for flow and heat transfer in two-dimensional fractured rocks: Chinese Journal of Rock Mechanics and Engineering, **33**, 43–51.

Collin, M., and D. Rowcliffe, 2002, The morphology of thermal cracks in brittle materials: Journal of the European Ceramic Society, **22**, 435–445, doi: 10.1016/S0955-2219(01)00319-3.

Fan, L., H. Li, and Y. Xi, 2022, Investigation of three different cooling treatments on dynamic mechanical properties and fragmentation characteristics of granite subjected to thermal cycling: Underground Space, 2467–9674, doi: 10.1016/j.undsp.2021.12.010.

Griffiths, L., O. Lengliné, M. J. Heap, P. Baud, and J. Schmittbuhl, 2018, Thermal cracking in westerly granite monitored using direct wave velocity, coda wave interferometry, and acoustic emissions: Journal of Geophysical Research: Solid Earth, **123**, 2246–2261, doi: 10.1002/2017JB015191.

Homand-Etienne, F., and R. Houpert, 1989, Thermally induced microcracking in granites: Characterization and analysis: International Journal of Rock Mechanics and Mining Sciences & Geomechanics Abstracts, **26**, 125–134, doi: 10.1016/0148-9062(89)90001-6.

Hu, J., H. Xie, C. Li, and Q. Sun, 2021, Effect of cyclic thermal shock on granite pore permeability: Lithosphere, Special **2021**, 4296301, doi: 10.2113/2021/4296301.

Johnston, K. P. and J. M. L. Penninger, eds., 1989, Supercritical Fluid Science and Technology: ACS Symposium Series, **406**, American Chemical Society, Washington, DC.

Junique, T., P. Vázquez, Y. Géraud, C. Thomachot-Schneider, and H. Sidibé, 2021, Microstructural evolution of granitic stones exposed to different thermal regimes analysed by infrared thermography: Engineering Geology, **286**, 106057, doi: 10.1016/j.enggeo.2021.106057.

Kaiser, E. J., 1950, A study of acoustic phenomena in tensile test: Ph.D. thesis: Technische Hochschule München.

Kang, F., T. Jia, Y. Li, J. Deng, and X. Huang, 2021, Experimental study on the physical and mechanical variations of hot granite under different

cooling treatments: Renewable Energy, **179**, 1316–1328, doi: 10.1016/j.renene.2021.07.132.

Kent, T., J. Louie, and J. Echols, 2013, Correlating azimuthal anisotropy to geothermal resource potential using a 3D-3C seismic survey of Soda Lake geothermal field, Nevada: 83rd Annual International Meeting, SEG, Expanded Abstracts, 341–346, doi: 10.1190/segam2013-1398.1.

Kumari, W. G. P., P. G. Ranjith, M. S. A. Perera, S. Shao, B. K. Chen, A. Lashin, N. A. Arifi, and T. D. Rathnaweera, 2017, Mechanical behaviour of Australian Strathbogie granite under in-situ stress and temperature conditions: An application to geothermal energy extraction: Geothermics, **65**, 44–59, doi: 10.1016/j.geothermics.2016.07.002.

Lehujeur, M., J. Vergne, J. Schmittbuhl, and A. Maggi, 2015, Characterization of ambient seismic noise near a deep geothermal reservoir and implications for interferometric methods: A case study in northern Alsace, France: Geothermal Energy, **3**, 1–17, doi: 10.1186/s40517-014-0020-2.

Lemmon, E. W., M. O. McLinden, and D. G. Friend, 2005, Thermophysical properties of fluid systems, *in* P. J. Lindstrom and W. G. Mallard, eds., NIST chemistry webbook 69: NIST Standard Reference Database.

Li, N. Q., W. B. Deng, L. Y. Fu, J. M. Carcione, and T. C. Han, 2022, Wave propagation in double-porosity thermoelastic media: Geophysics, **87**, no. 6, MR265–MR277, doi: 10.1190/geo2022-0008.1.

Li, N. Q., L. Y. Fu, J. Yang, and T. Han, 2021, On three-stage temperature dependence of elastic wave velocities for rocks: Journal of Geophysics and Engineering, **18**, 328–338, doi: 10.1093/jge/gxab017.

Lin, W., 2002, Permanent strain of thermal expansion and thermally induced microcracking in Inada granite: Journal of Geophysical Research: Solid Earth, **107**, ECV3-1–ECV3-16, doi: 10.1029/2001JB000648.

Lindroth, D. P., and W. G. Krawza, 1971, Heat content and specific heat of six rock types at temperatures to 1,000°C: US Bureau of Mines.

Majer, E. L., R. Baria, M. Stark, S. Oates, J. Bommer, B. Smith, and H. Asanuma, 2007, Induced seismicity associated with enhanced geothermal systems: Geothermics, **36**, 185–222, doi: 10.1016/j.geothermics.2007.03.003.

Mavko, G., and T. Mukerji, 1998, Comparison of the Krief and critical porosity models for prediction of porosity and V_P/V_S: Geophysics, **63**, 925–927, doi: 10.1190/1.1444403.

Mavko, G., T. Mukerji, and J. Dvorkin, 2003, The rock physics handbook: Cambridge University Press.

Olasolo, P., M. C. Juárez, M. P. Morales, and I. A. Liarte, 2016, Enhanced geothermal systems (EGS): A review: Renewable and Sustainable Energy Reviews, **56**, 133–144, doi: 10.1016/j.rser.2015.11.031.

Pai, N., F. Ju, H. J. Su, Z. Q. He, M. Xiao, Y. Z. Zhang, C. Zhou, and D. Wang, 2021, An investigation on the deterioration of physical and mechanical properties of granite after cyclic thermal shock: Geothermics, **97**, 102252, doi: 10.1016/j.geothermics.2021.102252.

Poletto, F., B. Farina, and J. M. Carcione, 2018, Sensitivity of seismic properties to temperature variations in a geothermal reservoir: Geothermics, **76**, 149–163, doi: 10.1016/j.geothermics.2018.07.001.

Qi, H., J. Ba, and T. M. Müller, 2021, Temperature effect on the velocity-porosity relationship in rocks: Journal of Geophysical Research: Solid Earth, **126**, e2019JB019317, doi: 10.1029/2019JB019317.

Robertson, E. C., 1988, Thermal properties of rocks: U.S. Geological Survey Open-File Report.

Salaun, N., H. Toubiana, J. B. Mitschler, G. Gigou, X. Carriere, V. Maurer, and A. Richard, 2020, High-resolution 3D seismic imaging and refined velocity model building improve the image of a deep geothermal reservoir in the Upper Rhine Graben: The Leading Edge, **39**, 857–863, doi: 10.1190/tle39120857.1.

Shi, X., L. Gao, J. Wu, C. Zhu, S. Chen, and X. Zhuo, 2020, Effects of cyclic heating and water cooling on the physical characteristics of granite: Energies, **13**, 2136, doi: 10.3390/en13092136.

Sultan, N., J. P. Foucher, P. Cochonat, T. Tonnerre, J. F. Bourillet, H. Ondreas, E. Cauquil, and D. Grauls, 2004, Dynamics of gas hydrate: Case of the Congo continental slope: Marine Geology, **206**, 1–18, doi: 10.1016/j.margeo.2004.03.005.

Sun, Q., Z. Q. Zhang, L. Xue, and S. Y. Zhu, 2013, High temperature phase transition and physical and mechanical properties of rock: Chinese Journal of Rock Mechanics and Engineering, **32**, 935–942.

Tian, H., Z. Zhu, P. G. Ranjith, G. Jiang, and B. Dou, 2021, Experimental investigation of drillability indices of thermal granite after water-cooling treatment: Natural Resources Research, **30**, 4621–4640, doi: 10.1007/s11053-021-09926-1.

Wang, F., T. Frühwirt, and H. Konietzky, 2020, Influence of repeated heating on physical-mechanical properties and damage evolution of granite: International Journal of Rock Mechanics and Mining Sciences, **136**, 104514, doi: 10.1016/j.ijrmms.2020.104514.

Wang, F., and H. Konietzky, 2019, Thermo-mechanical properties of granite at elevated temperatures and numerical simulation of thermal cracking: Rock Mechanics and Rock Engineering, **52**, 3737–3755, doi: 10.1007/s00603-019-01837-1.

Wang, F., and H. Konietzky, 2022, Thermal cracking in granite during a heating–cooling cycle up to 1000°C: Laboratory testing and real-time sim-

ulation: Rock Mechanics and Rock Engineering, **55**, 1411–1428, doi: 10.1007/s00603-021-02740-4.

Wang, H. F., B. P. Bonner, S. R. Carlson, B. J. Kowallis, and H. C. Heard, 1989, Thermal stress cracking in granite: Journal of Geophysical Research, **94**, 1745–1758, doi: 10.1029/JB094iB02p01745.

Wang, L. L., M. Bornert, E. Héripré, D. S. Yang, and S. Chanchole, 2014, Irreversible deformation and damage in argillaceous rocks induced by wetting/drying: Journal of Applied Geophysics, **107**, 108–118, doi: 10.1016/j.jappgeo.2014.05.015.

Wei, J., L. Y. Fu, Z. W. Wang, J. Ba, and J. M. Carcione, 2020, Green's function of the Lord–Shulman thermoporoelasticity theory: Geophysical Journal International, **221**, 1765–1776, doi: 10.1093/gji/ggaa100.

Willis, E., J. Bresee, B. D. Bona, J. Salisbury, J. T. Mock, A. Jelacic, P. Goldman, and L. R. Mink, 2010, A history of geothermal energy research and development in the United States: Geothermal Technologies Program, U.S. Department of Energy.

Yang, J., L. Y. Fu, B. Y. Fu, Z. W. Wang, and W. T. Hou, 2021, High-temperature effect on the material constants and elastic moduli for solid rocks: Journal of Geophysics and Engineering, **18**, 583–593, doi: 10.1093/jge/gxab037.

Yang, J., L. Y. Fu, F. Wang, and W. B. Deng, 2022a, Coupled thermo-mechanical damage evolution of granite under repeated heating-cooling cycles and the applications of Mohr-Coulomb and Drucker-Prager models: Natural Resources Research, **31**, 2629–2652, doi: 10.1007/s11053-022-10084-1.

Yang, J., L. Y. Fu, Y. Zhang, and T. Han, 2022b, Temperature-and pressure-dependent pore microstructures using static and dynamic moduli and their correlation: Rock Mechanics and Rock Engineering, **55**, 4073–4092, doi: 10.1007/s00603-022-02829-4.

Yang, J., L. Y. Fu, W. Q. Zhang, and Z. W. Wang, 2019, Mechanical property and thermal damage factor of limestone at high temperature: International Journal of Rock Mechanics and Mining Sciences, **117**, 11–19, doi: 10.1016/j.ijrmms.2019.03.012.

Yao, J., X. Zhang, C. Q. Huang, L. Gong, W. D. Yang, and Y. Li, 2022, Numerical simulation of thermo-hydraulic coupling process in fractured-vuggy karst geothermal reservoirs: Natural Gas Industry, **42**, 107–116.

Yao, J., X. Zhang, Z. Sun, Z. Huang, J. Liu, Y. Li, Y. Xin, X. Yan, and W. Liu, 2018, Numerical simulation of the heat extraction in 3D-EGS with thermal-hydraulic-mechanical coupling method based on discrete fractures model: Geothermics, **74**, 19–34, doi: 10.1016/j.geothermics.2017.12.005.

Ye, X., Z. Yu, Y. Zhang, J. Kang, S. Wu, T. Yang, and P. Gao, 2022, Mineral composition impact on the thermal conductivity of granites based on geothermal field experiments in the Songliao and Gonghe Basins, China: Minerals, **12**, 247, doi: 10.3390/min12020247.

Zhang, F., J. Zhao, D. Hu, F. Skoczylas, and J. Shao, 2018, Laboratory investigation on physical and mechanical properties of granite after heating and water-cooling treatment: Rock Mechanics and Rock Engineering, **51**, 677–694, doi: 10.1007/s00603-017-1350-8.

Zhang, X., Z. Huang, Q. Lei, J. Yao, L. Gong, Z. Sun, and Y. Li, 2021, Impact of fracture shear dilation on long-term heat extraction in enhanced geothermal systems: Insights from a fully-coupled thermo-hydro-mechanical simulation: Geothermics, **96**, 102216, doi: 10.1016/j.geothermics.2021.102216.

Zuberek, W. M., B. Zogala, R. Dubiel, and J. Pierwola, 2002, Maximum temperature memory in sandstone and mudstone observed with acoustic emission and ultrasonic measurements: International Journal of Rock Mechanics and Mining Sciences, **35**, 416–417, doi: 10.1016/S0148-9062(98)00115-6.

Biographies and photographs of the authors are not available.